

[This article is a preprint]

# Estimation of surface and deep flows from sparse SSH observations of geostrophic ocean turbulence using Deep Learning

Georgy E Manucharyan<sup>1</sup>, Lia Siegelman<sup>2</sup>, Patrice Klein<sup>2</sup>

<sup>1</sup>School of Oceanography, University of Washington, Seattle, WA, USA

<sup>2</sup>Jet Propulsion Laboratory, California Institute of Technology, Pasadena, CA, USA

## Key Points:

- A Deep Learning framework is developed to estimate mesoscale ocean currents from temporally-sparse SSH observations
- The Deep Learning framework outperforms linear and dynamical SSH interpolation techniques.
- A skillful state estimation of unobserved deep flows from SSH observations is achieved via supervised Deep Learning

---

Corresponding author: Georgy Manucharyan, [gmanuch@uw.edu](mailto:gmanuch@uw.edu)

**Abstract**

Satellite altimeters provide global observations of sea surface height (SSH) and present a unique dataset for advancing our theoretical understanding of upper ocean dynamics and monitoring its variability. Considering that mesoscale SSH patterns of 50–300 km in size can evolve on timescales comparable to or shorter than satellite return periods, it is challenging to accurately reconstruct the continuous SSH evolution as currently available altimetry observations are still spatially and temporally sparse. Here we explore the possibility of SSH interpolation via a Deep Learning framework using synthetic observations from a quasigeostrophic model of mesoscale ocean turbulence. We demonstrate that Convolutional Neural Networks with Residual Learning are superior in SSH reconstruction to linear and recently developed dynamical interpolation techniques. In addition, neural networks can provide a skillful state estimate of unobserved deep ocean currents at mesoscales. This conspicuous result suggests that SSH patterns of eddies do contain substantial information about the underlying deep ocean currents that is necessary for SSH prediction. Our framework is highly idealized and several crucial improvements such as transfer learning, diversification of training data, and modification of the loss function would be necessary to implement before its ultimate use with real satellite observations. Nonetheless, by providing a proof of concept based on synthetic data, our results point to Deep Learning as a viable alternative to existing interpolation and, more generally, state estimation methods for satellite observations of eddying currents.

**Plain Language Summary**

Satellite observations of sea surface height (SSH) are widely used to derive surface ocean currents on a global scale. However, due to gaps in SSH observations, it remains challenging to retrieve the dynamics of rapidly evolving upper-ocean currents. To overcome this limitation, we propose a Deep Learning framework that is based on pattern recognition extracted from SSH observations. Using synthetic data generated from a simplified model of ocean turbulence, we demonstrate that Deep Learning can accurately estimate both surface and sub-surface ocean currents, significantly outperforming the most commonly used techniques. By providing a proof of concept, our study highlights the strong potential of Deep Learning for estimating ocean currents from satellite observations.

## 1 Introduction

Satellite-derived global observations of sea surface height (SSH) have shed light on many dynamical processes including large-scale circulation, propagation of waves, and the evolution of the mesoscale eddy field (Chelton et al., 2011; Fu et al., 2010). Since the satellite era, an increasing amount of evidence points towards mesoscale eddies being a key component of the global ocean circulation and the Earth’s climate as a whole due to their influence on mean currents, heat and salt transport, atmosphere-ocean interactions, and biological productivity (Ferrari & Wunsch, 2009; Klein et al., 2019). Nonetheless, understanding and monitoring the oceanic kinetic energy spectrum and the associated spectral energy fluxes (Scott & Arbic, 2007; Aluie et al., 2018), understanding tracer dispersion (Abernathey & Marshall, 2013) or inferring subsurface flows (Klein et al., 2009) remain challenging because these quantities depend on higher-order SSH derivatives that are resolution-sensitive.

To increase the density of SSH observations, several altimeters have been put in orbit but their 10-20 days repeat orbits and relatively coarse along-track resolutions allow to view the ocean dynamics only down to relatively large mesoscale eddies of  $O(100)$  km wavelengths (Wunsch, 2010; Chelton & Schlax, 2003). The upcoming Surface Water Ocean Topography (SWOT) altimeter mission (Fu & Ubelmann, 2014) promises to observe ocean mesoscale eddies and submesoscale fronts ( $\leq 50$  km) at unprecedented spatial resolutions, potentially resolving 15-30km wavelengths. However, with its complete repeat cycle of 21 days, the temporal resolution of the altimeter is insufficient to continuously capture the evolution of submesoscale eddies, although the mesoscale eddy field can be partially resolved in both space and time if data from several altimeters are used. The mismatch between the high spatial resolution and the moderate temporal resolution presents a challenge for reconstructing time-continuous maps of SSH. The SSH interpolation can be especially challenging in regions with energetic baroclinic turbulence where the evolution of small-scale SSH anomalies can be fast compared to the satellite return periods, e.g. in such major currents as the Antarctic Circumpolar Current, Kuroshio Extension, and Gulf Stream.

The existing gridded SSH products, e.g. AVISO (Ducet et al., 2000), are spatially and temporally interpolated from the along-track altimetry measurements and hence their accuracy and effective resolution are constrained by the density of observations and deficiencies of the interpolation technique. The temporal SSH interpolation could be conceptually viewed as reconstructing the phase-space trajectory given only partial observations of the two endpoints separated in time. A major complication arises due to the chaotic nature of ocean turbulence in which phase-space trajectories can be so well-mixed that there is a large number of plausible trajectories passing within some close vicinity of any given endpoints. Thus, the task of temporal interpolation, i.e. finding the true trajectory, becomes increasingly more difficult with an increasing time separation between observations. Most commonly used interpolation techniques, such as objective mapping or polynomial interpolation, do not attempt to make use of any potential dynamical constraints present in the data and perform well only for autocorrelated data while failing for sparse data. It is thus crucial to develop frameworks to efficiently extract information about the oceanic eddy dynamics from the spatially and temporally sparse SSH observations. Below we discuss how the nature of baroclinic ocean turbulence can provide dynamical limitations for SSH interpolation and why Deep Learning might be a viable alternative to other interpolation techniques.

### 1.1 SSH interpolation and the associated dynamical limitations

Spatiotemporal interpolation or gridding of SSH data is inherently linked to ocean physics as the success of a given technique ultimately should rely on the pertinence of its assumed model (either dynamical or statistical) that captures the essence of eddy propagation in space and time. To illustrate this point, imagine a coherent eddy moving in a turbulent field and several altimeter tracks passing through it at different times and directions. If

97 there is an accurate model of eddy propagation, it would allow pinpointing the observations  
 98 taken over this specific eddy and combining this information to better constrain the two-  
 99 dimensional eddy shape. Thus, to extract the information from various altimetry tracks to  
 100 the fullest extent, it is necessary to have an accurate model of eddy evolution. However, due  
 101 to the stratified nature of geostrophic ocean turbulence, the unobserved deep ocean flows  
 102 can affect the surface dynamics, and hence the SSH observations on their own may not be  
 103 self-sufficient to infer its evolution. Given the lack of subsurface information at eddy scales,  
 104 constructing a closed system of equations for SSH evolution is challenging.

105 Another complication for SSH interpolation arises due to the chaotic nature of baro-  
 106 clinic turbulence that implies an increasingly high sensitivity to initial conditions as time  
 107 progresses. Alternatively, with increasing time-separation between any two observations, the  
 108 relation between them becomes more convoluted because the phase-space trajectories are  
 109 well-mixed. Thus, at sufficiently large separation times, one could effectively treat observa-  
 110 tions as independent samples, and hence interpolating between these observations would not  
 111 be plausible. While the chaos itself makes the connections between subsequent observations  
 112 highly nonlinear, combined with the fact that satellites only provide approximate and par-  
 113 tial observations of the ocean, the temporal SSH interpolation becomes under-constrained,  
 114 i.e. it might not have unique solutions as not enough information is given.

115 Existing methods for spatiotemporal SSH interpolation can be broadly split into two  
 116 distinct classes: methods that rely on a postulated dynamical model of SSH evolution and  
 117 purely data-driven methods. Both methods have their advantages and disadvantages. To  
 118 avoid prescribing a dynamical model, statistical models like objective interpolation (Davis,  
 119 1985; Le Traon et al., 1998; Ducet et al., 2000) rely on data only. Their premise is to in-  
 120 corporate spatiotemporal correlations and measurement error into a statistical model and  
 121 provide the most likely estimate of the true continuous field under consideration. However,  
 122 this method does not rely on any dynamical model of the eddy propagation and hence can  
 123 lead to an unphysical behavior of the interpolated SSH field. Methods involving dynamical  
 124 ocean models are typically based on data assimilation, a procedure that minimizes the differ-  
 125 ence between the observed and modeled fields by adjusting unknown variables like boundary  
 126 and initial conditions or external forcing (see e.g. reanalysis product by Carton & Giese,  
 127 2008). While resulting in SSH fields that are dynamically-constrained, this method suffers  
 128 from a drawback that it requires additional observations to constrain other essential model  
 129 variables like the subsurface flow and/or the density field. Also, data assimilation for com-  
 130 plex ocean models at eddy-resolving scales is often under-determined and is computationally  
 131 demanding.

132 A recent study by Ubelmann et al. (2015) demonstrated that representing SSH prop-  
 133 agation with a single equivalent barotropic mode in a quasigeostrophic model results in  
 134 significant improvements in the spatiotemporal interpolation of sparse SSH observations. In  
 135 particular, Ubelmann et al. (2015) considered a fundamental problem of reconstructing the  
 136 SSH distribution that occurred in between two observed SSH fields separated by about 20  
 137 days, a characteristic timescale required by a set of altimeters to reconstruct a spatial SSH  
 138 field. They found that integrating the earlier SSH observation forward in time (following  
 139 the assumed dynamics of an equivalent barotropic mode) and averaging it with the later  
 140 observed SSH anomalies that were integrated backward in time resulted in an improvement  
 141 compared to conventional linear interpolation methods. In follow-up work, Ubelmann et al.  
 142 (2016) generalized this temporal interpolation method to the spatiotemporal interpolation  
 143 of along-track SSH observations by essentially performing data-assimilation on the one-layer  
 144 QG model. The advantage of the dynamical interpolation method is that it relies on the  
 145 advection of potential vorticity – a non-linear process that is inherently present in ocean  
 146 dynamics and cannot be represented by linear or objective interpolation techniques.

147 A drawback of the dynamical interpolation is that it assumes that SSH evolves indepen-  
 148 dently of deep ocean flows, considering the so-called equivalent barotropic mode dynamics  
 149 (Berloff & Meacham, 1997). However, in many energetic regions of the ocean, e.g. in Gulf

150 Stream, Kuroshio or Antarctic Circumpolar Current, the currents are baroclinically unstable  
 151 and hence are necessarily composed of at least two dynamically interacting vertical modes,  
 152 the barotropic and baroclinic modes (see e.g. Chapter 6 in Vallis, 2017). To illustrate this  
 153 point, consider the conservation of quasigeostrophic potential vorticity  $q_1$  in the upper ocean  
 154 layer as a model of SSH evolution at mesoscales:

$$155 \quad \frac{Dq_1}{Dt} = \underbrace{\frac{D}{Dt}[\nabla^2\psi_1 - R_d^{-2}\psi_1 + \beta y]}_{\text{Depends on partially-observed } \psi_1} + \underbrace{R_d^{-2} \frac{D}{Dt}\psi_{b.t.}}_{\text{Depends on unobserved } \psi_2} \approx 0, \quad (1)$$

$$156 \quad \text{where } \psi_{b.t.} = \frac{H_1\psi_1 + H_2\psi_2}{H_1 + H_2} \text{ and } R_d^{-2} = \frac{f_0^2}{g'H_1} + \frac{f_0^2}{g'H_2}, \quad (2)$$

$\psi_1$  and  $\psi_2$  are the surface and deep ocean stream functions,  $\psi_{b.t.}$  is the barotropic stream-function (depth-averaged transport),  $R_d$  is the Rossby baroclinic deformation radius,  $f_0$  and  $\beta$  are the Coriolis and beta-plane parameters,  $y$  is the meridional coordinate,  $H_1$  and  $H_2$  are the ocean layer depths,  $g'$  is the reduced gravity, and  $D/Dt$  is the material derivative accounting for advection by the surface flow (see Methods). Note that the surface stream-function is directly proportional to SSH:  $\psi_1 = (g/f_0)SSH$ , where  $g$  is the acceleration due to gravity. On relatively short timescales, sources and dissipation of potential vorticity could be neglected and its approximate conservation provides a basic description of the eddy evolution. The terms in the equation 1 above have been grouped into those that only depend on the partially-observed  $\psi_1$  (or equivalently SSH) and terms that depend on the unobserved subsurface flow  $\psi_2$  (or on the barotropic flow  $\psi_{b.t.}$ ). By considering only the equivalent barotropic mode dynamics and taking  $\psi_1$  to be equal to the baroclinic mode, the dynamical interpolation method as described in Ubelmann et al. (2015, 2016) discards the term in the PV conservation equation that depends on the unobserved barotropic streamfunction, resulting in

$$\frac{D}{Dt}[\nabla^2\psi_1 - R_d^{-2}\psi_1 + \beta y] = 0. \quad (3)$$

157 Since the discarded term is the only term that depends on the unknown streamfunction  $\psi_2$ ,  
 158 it is possible to integrate the approximate PV-conservation equation forward and backward  
 159 in time given only  $\psi_1$  observations, as was done in Ubelmann et al. (2015). Even though  
 160 in many ocean regions both deep and surface geostrophic currents are dynamically active,  
 161 reconstructing SSH using the dynamical interpolation technique proved to be superior to linear  
 162 interpolation methods (Ubelmann et al. (2015)) because it relies, at least approximately,  
 163 on the fundamental PV-conservation constraint. Nonetheless, the dynamical interpolation  
 164 method can lead to significant errors (see Results), implying that the omitted term, while  
 165 being relatively small, can substantially impact SSH evolution on timescales comparable to  
 166 return periods of altimetry satellites.

## 167 1.2 The rationale for Deep Learning approach.

168 A clear way of improving the dynamical interpolation algorithm would be to take into  
 169 account the contribution of the barotropic mode to SSH evolution. However, comprehensive  
 170 measurements of deep ocean currents at eddy scales are missing, posing a significant  
 171 challenge of inferring them from only SSH observations. Without taking into consideration  
 172 the physical processes that have led to the generation of any given SSH snapshot, there is a  
 173 wide range of plausible ways in which  $\psi_1$  could be decomposed into baroclinic and barotropic  
 174 modes, each corresponding to the distinct configuration of PV anomalies in the deep and  
 175 surface layers. However, considering that PV anomalies are specifically due to baroclinic  
 176 instabilities obeying specific conservation laws (Eq. 1), the corresponding barotropic and  
 177 baroclinic modes are inherently entangled, providing at least partial constraints on how any  
 178 specific SSH pattern could be partitioned into modes.

179 Since the QG model exhibits a highly non-linear and chaotic behavior, an analytical  
 180 approach to disentangle the modes has not been found but the evidence that data-driven

181 approach might be relevant has been presented in the literature. In particular, the surface  
 182 and subsurface flows from mooring observations are significantly correlated such that a  
 183 single Empirical Orthogonal Function (EOF) can explain a significant amount of variance  
 184 of the overall vertical velocity profile (Wunsch, 1997; de La Lama et al., 2016). Furthermore,  
 185 machine learning techniques such as self-organizing maps (Chapman & Charantonis, 2017),  
 186 as well as convolutional neural networks (Bolton & Zanna, 2019), have been successfully used  
 187 to estimate the subsurface flows from SSH data. However, the unknown term  $D\psi_{bt}/Dt =$   
 188  $(\partial_t + \mathbf{u}_1 \cdot \nabla)\psi_{bt}$  in Eq. 1 can only provide a substantial contribution to the PV budget if  $\psi_{bt}$   
 189 has a substantial component that is decorrelated from  $\psi_1$  because  $\mathbf{u}_1 \cdot \nabla\psi_1 \equiv 0$ , and  $\partial_t\psi_{bt} \ll$   
 190  $\partial_t\psi_1$  for surface-amplified flows. Thus the key for a more accurate SSH interpolation lies  
 191 in estimating the component of  $\psi_2$  that is decorrelated from  $\psi_1$  – a problem that is tightly  
 192 linked to estimating eddy heat fluxes in baroclinically unstable flows. Using residual neural  
 193 networks, George et al. (2019) demonstrated that  $\psi_1$  indeed contains substantial information  
 194 about the decorrelated part of the subsurface streamfunction  $\psi_2$ , allowing to estimate about  
 195 60% of the variance in eddy heat fluxes only from SSH snapshots. Given that machine  
 196 learning methods can extract information from SSH patterns to estimate the component of  
 197  $\psi_{bt}$  that is uncorrelated with  $\psi_1$  for estimation of the eddy heat fluxes, it is plausible that  
 198 they could be used for SSH interpolation as well.

199 While ocean turbulence is chaotic and appears to be random and unpredictable, it does  
 200 not prohibit characteristics that are particularly beneficial for deep learning: the emergence  
 201 of underlying repeating patterns, self-similarities, and self-organization. We thus hypoth-  
 202 esize that deep learning techniques could outperform conventional interpolation methods  
 203 including linear and dynamical interpolation. In this manuscript we use synthetic model  
 204 observations to present a proof of concept for using deep learning to shortcut the formal  
 205 process of data assimilation and reconstruct not only the interpolated SSH field but also the  
 206 corresponding unobserved deep ocean currents, thus providing a complete state estimate of  
 207 the baroclinic ocean turbulence.

208 The manuscript is organized in the following way. In Section 2, we present a range of  
 209 deep neural network architectures, outline a set of training experiments, and describe the  
 210 synthetic model of ocean turbulence that we used to evaluate the efficacy of Deep Learning  
 211 in SSH interpolation and state estimation of both surface and deep ocean streamfunctions.  
 212 In Section 3, we present examples of SSH estimates using deep neural networks and compare  
 213 their skills to linear and dynamical interpolation techniques. In Section 4, we discuss the  
 214 broader implications of our results, outline the deficiencies and advantages of our Deep  
 215 Learning methodology, and propose possible improvements to generalize our method for its  
 216 ultimate use with real satellite observations.

## 217 2 Methods

218 We implement a range of deep neural network architectures to address a basic question  
 219 of interpolating SSH fields in baroclinic ocean turbulence. To exclude potential limitations  
 220 of real-world data, our study is entirely based upon synthetic data that we generate using  
 221 the quasigeostrophic (QG) model of baroclinic ocean turbulence. We find the QG model  
 222 to be optimal for our goals as it is pertinent to many energetic regions in the ocean while  
 223 being relatively simple such that a large volume of data can be generated for training and  
 224 testing; furthermore, the model allows us to directly benchmark deep learning against the  
 225 dynamical interpolation technique that also utilizes QG dynamics. Below we describe our  
 226 neural network architectures, the QG model used for the generation of training and testing  
 227 datasets, and the details of the dynamical interpolation that we implemented for direct skill  
 228 comparisons with deep learning and linear interpolation.

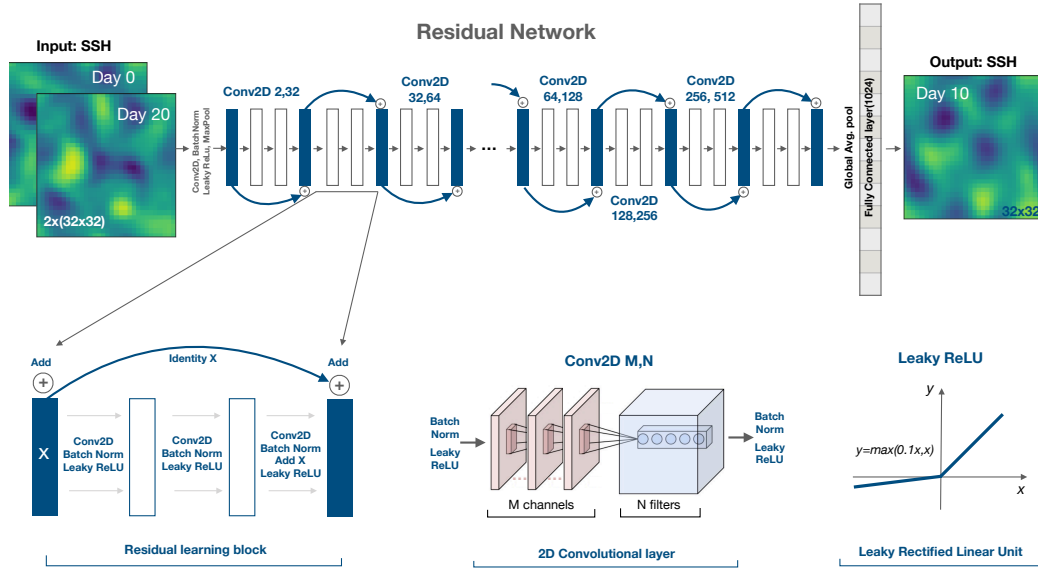


**Figure 1.** The ResNet architecture of a deep convolutional neural network with residual learning that was used for SSH interpolation and state estimation. The input consists of two SSH snapshots separated by 20 day. A set of convolutional layers are then applied to create an abstract representation of the input patterns in a bottleneck fashion: when image sizes decrease by a factor of two, the number of filters increases by a factor of two. Each convolutional layer is followed by the batch normalization and the application of the nonlinear function (Leaky Rectified Linear Unit). Residual learning blocks are saving the information from one layer and adding its identity to the output several layers ahead (blue arrows). The output from the final convolutional layer is subject to a global average pooling and flattening into a vector that is densely connected to the output of the appropriate dimension to represent either a single or multiple fields.



## 2.1 Deep Learning framework: Residual Convolutional Neural Networks

Artificial neural networks are based on the idea of approximating the ‘output’ by taking the ‘input’ variable and performing a large number of matrix additions and multiplications, applying non-linearity functions, and either condensing or expanding the variable dimension as it passes from layer to layer. The resulting network contains a large number of free parameters that are later adjusted to optimize a given loss function, commonly taken as a measure of difference between the prediction and the truth. Because we are trying to extract information from the eddy patterns expressed in SSH fields, the choice of convolutional neural networks (CNNs) is rationalized. In passing the information from layer to layer, CNNs define a set of filters (kernel matrices with prescribed dimensions) and convolve images to produce increasingly more abstract levels of information that are passed on to the next layer. Here we implement the ResNet architecture – a Convolutional Neural Network with Residual Learning blocks (He et al., 2016). The Residual Learning is a process by which the information is not only transferred sequentially from one layer to another but is also transferred by skipping several layers via the so-called skip connections (blue arrows in Fig. 1). The presence of skip connections can result in better performances for a wide range of computer vision problems (Targ et al., 2016). An example of the open-source implementation of the ResNet architecture in Keras following He et al. (2016) was provided by Michael Dietz here <https://gist.github.com/mjdietzx/0cb95922aac14d446a6530f87b3a04ce>, and we have adjusted this code for our specific problem of SSH interpolation and state estimation.

A brief description of the ResNet architecture as shown schematically in Figure 1 follows. The input consists of two SSH snapshots represented by a  $(32,32,2)$  matrix. The very first convolutional layer takes the input and applies a set of 32 convolutional filters of size  $(5,5)$  with a stride of  $(1,1)$ , followed by the batch normalization, the nonlinearity function taken to be the Leaky Rectified Linear Unit (Leaky ReLU), and the maximum 2D pooling of size  $(2,2)$  with a stride of  $(2,2)$ . Next, a series of residual learning blocks follow, each consisting of two convolutional layers that take the input with  $M$  channels and apply  $N$  filters, each followed by batch normalization and Leaky ReLU, and at the very end of the residual block, its initial input matrix is added to its output (see Figure 1). The architecture has a total of 16 residual blocks containing 52 convolutional layers. The first series of residual blocks consist of 3 blocks that transform the input from  $M = 32$  to  $M = 64$  channels while reducing the matrix rows and columns by a factor of two using the  $(2,2)$  max pooling. Next, a set of 4 blocks transform the input to 128 channels, a set of 6 blocks to 256, and a set of 3 blocks to 512 channels, and the matrix dimension becomes  $(2,2,512)$ . Then, a global two-dimensional average pooling is applied to have a vector of length 512, which is in some experiments subjected to a dropout rate of 20%. The resulting vector is then densely connected to a vector of size 1024, which is finally reshaped to represent the output SSH snapshot of size  $(32,32)$ . For our state estimation experiments with 4 separate fields appearing as the output matrix, the ResNet architecture remains the same except for the final dense layer being of length 4096 and reshaped to the appropriate output size of  $(32,32,4)$ .

We have explored more complex ResNets (going up to 161 convolutional layers) but also simpler CNN architectures without residual learning as well as shallow feed-forward networks (see Table 1). A brief description of the neural network architectures follows. **FC**: feed-forward neural network with 2 hidden layers (254 and 512 neurons correspondingly), batch normalization, and leaky ReLU as an activation function after each hidden layer. **FC\_Large**: same as **FC** but with 512 and 1024 neurons in the hidden layers. **VGG**: convolutional neural network with 32  $(4 \times 4)$  filters in the first layer, 64  $(3 \times 3)$  in the second, 128  $(3 \times 3)$  in the third, 256  $(2 \times 2)$  in the fourth, with batch normalization and leaky ReLU used after each layer and the two-dimensional global average pooling before connecting to the dense layer. **VGG\_Large**: same as **VGG** but using a four times larger number of filters in each convolutional layer. **VGG\_Deep**: same as **VGG** but repeating each convolutional layer 3 times before proceeding to the next one. **ResNet\_Small**, **ResNet**,



282 **and ResNet\_Large** are residual neural networks with architectures as depicted in Figure 1  
 283 but with a total of 31,52, and 161 convolutional layers correspondingly; **\_Dropout** denotes  
 284 the use of 20% dropout rate in the last layer. We have implemented the architectures  
 285 in Tensorflow/Keras and provided the Python scripts along with the training data in the  
 286 Zenodo data repository (Manucharyan, 2020).

#	Architecture	Parameters	Data Samples	$\Delta T$ (days)	Skill
1	FC	$1.2 \times 10^6$	$2 \times 10^5$	20	0.53
2	FC_Large	$6.3 \times 10^6$	$2 \times 10^5$	20	0.54
3	VGG	$0.5 \times 10^6$	$2 \times 10^5$	20	0.63
4	VGG_Large	$4.6 \times 10^6$	$2 \times 10^5$	20	0.64
5	VGG_Deep	$1.4 \times 10^6$	$2 \times 10^5$	20	0.61
6	ResNet_Small	$0.9 \times 10^6$	$2 \times 10^5$	20	0.69
7	ResNet_Large	$7 \times 10^6$	$2 \times 10^5$	20	0.72
8	ResNet_Large_Dropout	$7 \times 10^6$	$2 \times 10^5$	20	0.72
9	ResNet_Dropout	$4.7 \times 10^6$	$2 \times 10^5$	20	0.73
10	ResNet	$4.7 \times 10^6$	$2 \times 10^5$	20	0.75
11	ResNet	$4.7 \times 10^6$	$2 \times 10^5$	40	0.44
12	ResNet	$4.7 \times 10^6$	$2 \times 10^5$	60	0.18
13	ResNet	$4.7 \times 10^6$	$1 \times 10^5$	20	0.71
14	ResNet	$4.7 \times 10^6$	$4 \times 10^4$	20	0.65
15	ResNet	$4.7 \times 10^6$	$2 \times 10^4$	20	0.58
16	ResNet	$4.7 \times 10^6$	$8 \times 10^3$	20	0.55
17	ResNet	$4.7 \times 10^6$	$4 \times 10^3$	20	0.44
18	ResNet	$4.7 \times 10^6$	$1 \times 10^3$	20	0.39
19	ResNet	$4.7 \times 10^6$	$5 \times 10^2$	20	0.33

**Table 1.** List of neural network training experiments demonstrating the achieved prediction skill for temporal interpolation of SSH snapshots. Experiments 1-10 explore various architectures, 11-12 explore the skill deterioration with increasing time separation between the input images, and 13-19 explore skill dependence on the number of training examples. The architecture names correspond to function names in the provided NetworkArchitectures.py script that encodes their graphs using TensorFlow/Keras. The parameters column represents the number of trainable neural network parameters for corresponding architectures. The Data Samples column denotes the number of input-output examples that were used in neural network training. The  $\Delta T$  column denotes the time separation between the two input snapshots of SSH, and the skill column denotes the maximum achieved skill on validation data.

287 As a performance metric we define the model skill that is proportional to the loss  
 288 function and normalized by the standard deviation of the SSH signal in the following way:

$$289 \quad Skill = 1 - \left( \frac{|SSH_{predicted} - SSH_{true}|^2}{|SSH_{true}|^2} \right)^{\frac{1}{2}}. \quad (4)$$

290 For reference, the maximum skill=1 is achieved when the predicted and true images are  
 291 identical; the skill=0 corresponds to a prediction that makes the same error as assuming a  
 292 spatially homogeneous SSH field, and negative skill implies an even worst fit. This definition  
 293 of skill is more conservative than the correlation coefficient or the R-squared value; for

294 example,  $\psi_2$  is correlated to  $\psi_1$  with an average correlation coefficient of 0.74 and the linear  
 295 regression model has the R-squared of about 0.55 but the skill is only 0.33 if defined as in  
 296 equation 4 above. It is thus important to compare the results from different publications  
 297 using consistent metrics. Here we use the skill metric that is based on the RMS-error  
 298 normalized by the standard deviation (Eq. 4) and, for consistency, we use the Mean Square  
 299 Error (L2 norm) as the loss function for a neural network to minimize during training.

300 Coefficients of filter matrices, along with all other weights and biases involved in the neural  
 301 network architecture are then iteratively optimized using the Adam optimizer (Kingma  
 302 & Ba, 2014) to minimize the loss function that is the root-mean-square difference between  
 303 the predicted and true SSH images (or equivalently to maximize the skill). The parameter  
 304 optimization procedure requires evaluating neural network predictions for a large volume of  
 305 training data and hence the final optimized state of a particular neural network depends  
 306 only on the training data itself. To ensure that no overfitting have occurred, the neural network  
 307 skill is evaluated for a group of three independent datasets: training, validation, and  
 308 testing. The training data are used only for the training purposes, the validation data are  
 309 used to evaluate the skill of the neural network and to identify a stoppage criterion for the  
 310 training, while the testing data are used at the very last step to define the skill of a trained  
 311 neural network. All three datasets are generated from different numerical simulations to  
 312 ensure that overfitting didn't occur.

## 313 2.2 Synthetic training data: quasigeostrophic model

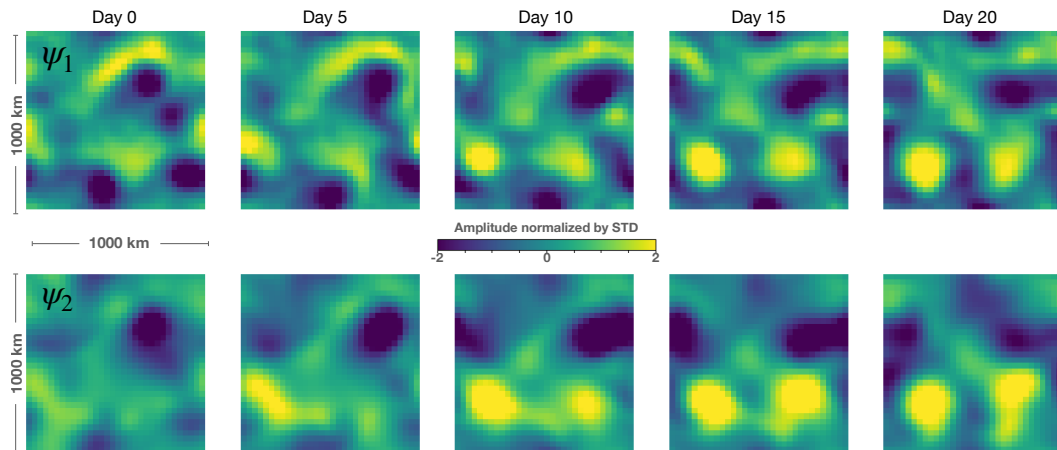


**Figure 2.** An example of the eddy field evolution over 20 days as generated by the QG model of a baroclinically unstable current. Top panels show surface streamfunction  $\psi_1$  (or SSH) and bottom panels show the corresponding deep ocean streamfunction  $\psi_2$ , both being normalized by their respective standard deviations; the domain size is 1000x1000 km and rows correspond to streamfunction snapshots taken five days apart. Note that the eddy field dramatically changes over 20 days (SSH decorrelation time scale is about 10–20 days), implying that conventional linear or optimal interpolation methods would lead to significant errors if available observations are separated by more than the decorrelation timescale.

314 In the absence of high-quality and/or large volumes of data, neural networks are likely  
 315 to overfit the training data and have poor skills when evaluated on the test data. To  
 316 avoid these issues we choose to train neural networks on synthetic data generated using an  
 317 idealized model of ocean turbulence – the two-layer quasigeostrophic (QG) model (Phillips,  
 318 1951; Vallis, 2017). The QG model is pertinent to baroclinically unstable flow and contains

319 the propagation dynamics of large-scale ocean eddies, including advection by the mean  
 320 flow, the beta drift, and the eddy interactions with the mean flow. Our choice of using the  
 321 two-layer model is rationalized because i) ocean currents are predominantly composed of  
 322 the barotropic and the first baroclinic mode (Wunsch, 1997; Smith & Vallis, 2001) and ii)  
 323 it is the minimal model demonstrating the difficulty of predicting SSH evolution without  
 324 direct observations of subsurface flows because both layers are necessarily dynamically active  
 325 during baroclinic instabilities, and iii) the dynamical interpolation method also relies on QG  
 326 dynamics, allowing to make a straight-forward performance comparison.

327 The quasigeostrophic model relies on the conservation of potential vorticity and simu-  
 328 lates the mesoscale turbulence driven by baroclinic instabilities associated with the vertical  
 329 shear of the mean flow, requiring a minimum of two vertically stacked shallow layers. The  
 330 conservation laws for the top and bottom layer potential vorticities,  $q_{1,2}$ , are written in the  
 331 following way:

$$332 \quad \frac{Dq_1}{Dt} = \frac{D}{Dt} \left[ \nabla^2 \psi_1 - \frac{f_0^2}{g'H_1} (\psi_1 - \psi_2) + \beta y \right] = 0 \quad (5)$$

$$333 \quad \frac{Dq_2}{Dt} = \frac{D}{Dt} \left[ \nabla^2 \psi_2 - \frac{f_0^2}{g'H_2} (\psi_2 - \psi_1) + \beta y \right] = -r_{Ek} \nabla^2 \psi_2, \quad (6)$$

334 where  $\psi_{1,2}$  is the top and bottom layer streamfunctions,  $f_0$  is the Coriolis parameter and  
 335  $\beta$  is its derivative in the meridional  $y$ -direction,  $g'$  is the reduced gravity,  $D/Dt = \partial/\partial t +$   
 336  $\mathbf{u}\nabla$  is the material derivative using corresponding layer' geostrophic velocity  $u$ , and  $r_{Ek}$   
 337 is the bottom drag coefficient. The relative importance of the discarded term in the PV-  
 338 conservation budget in Eq. 1,  $D\psi_{bt}/Dt$ , could be estimated by comparing its magnitude to  
 339  $D\psi_1/Dt$ , where both material derivatives use the velocity in the top layer. The ratio of these  
 340 terms would scale roughly as the ratio of the characteristic amplitudes of the barotropic and  
 341 surface streamfunctions, which we find from numerical simulations to scale as the ratio of  
 342 layer depths in QG simulations of the baroclinic instabilities, i.e.  $[\bar{\psi}_{b.t.}^2/\bar{\psi}_1^{21}]^{\frac{1}{2}} \sim O(H_1/H_2)$ .  
 343 Since in most ocean regions the pycnocline is relatively shallow compared to the full depth  
 344 of the ocean, the flows are surface-amplified and the discarded term is relatively small but  
 345 non-negligible and can substantially impact the SSH evolution leading to significant errors  
 346 of the dynamical interpolation (see Results).

347 The QG model has been configured to represent baroclinically unstable currents such  
 348 as the Gulf Stream, Kuroshio, or Antarctic Circumpolar Current. Model parameters are  
 349 as follows: the Rossby deformation radius is 40 km, the ratio of mean layer depths is 0.2,  
 350 there is a steady uniform mean vertical shear of 0.2 m/s, beta plain parameter corresponds  
 351 to a latitude of 40 degrees, linear Ekman friction was prescribed in the bottom layer for  
 352 dissipation, and high-wavenumber motions are being filtered in Fourier space for all variables  
 353 (more details could be found in Flierl (1978); Arbic et al. (2012)). The model domain is  
 354 1000 km by 1000 km and periodic boundary conditions are used. We have explored various  
 355 resolutions and find that it is sufficient to use a relatively coarse grid of 32x32 to simulate  
 356 baroclinic instabilities and the chaotic evolution of relatively large mesoscale eddies. The  
 357 QG model is integrated forward in time managing an ensemble of noisy initial conditions  
 358 to produce a large volume of data: about 200,000 SSH snapshots separated by 10 days  
 359 (Figure 2). Over a timescale of 20 days, the correlation between SSH fields drops to about  
 360 0.4 and it is hard to identify any persisting eddies because their shapes and intensities have  
 361 dramatically changed due to interactions with other eddies (Figure 2). We ensure that the  
 362 data for training, validation, and testing come from distinct simulations to accurately access  
 363 the generalization skill of the neural network.

364 To evaluate the efficacy of neural networks, we consider the tasks of i) temporal interpo-  
 365 lation where the input consists of two SSH snapshots separated by 20 days, ii) spatiotemporal  
 366 interpolation with the same input as for the temporal interpolation but with SSH images  
 367 having missing data, and iii) the state estimation of unobserved deep ocean flows from SSH  
 368 snapshots. For the temporal separation of SSH images, we choose 20 days because it is of

369 the order of the return periods for existing altimeters and to be consistent with Ubelmann  
 370 et al. (2015), and we explore how the skill varies with increasing this timescale to 40 and  
 371 60 days (Table 1). For the spatiotemporal interpolation, we choose the area of missing data  
 372 to roughly correspond to that of the SWOT observations over its return period. For a 1000  
 373 km domain, SWOT would have about four crossings (each having a swath of 120 km) with  
 374 one inclination angle and another four with an opposite angle (see e.g. Figure 1 in Gaultier  
 375 et al. (2016)). While SWOT would have missing-data areas in the shape of a rhombus, here  
 376 for simplicity we have prescribed square shapes as there is no reason to assume this would  
 377 lose generality.

### 378 **2.3 Dynamical Interpolation**

379 We reproduce the dynamical interpolation methodology as outlined in Ubelmann et al.  
 380 (2015) and evaluate its skill distribution. The method consists of initializing the surface  
 381 streamfunction  $\psi_1 = (g/f_0)SSH$  and integrating a single-layer quasi-geostrophic equation,  
 382 i.e. Eq. 3. The domain size, boundary conditions, stratification parameters, and all other  
 383 parameters of the single-layer model are consistent with those of the two-layer model that  
 384 was used to generate the validation data. The model integration is performed for 10 days  
 385 forward in time starting from the SSH snapshot on day 0 and also backward in time starting  
 386 from the SSH snapshot on day 20. The backward in time integration is performed by  
 387 reversing the direction of the velocity field and changing the time variable to be negative.  
 388 The estimate of the SSH field on day 10 is then taken to be the arithmetic mean between  
 389 the SSH fields resulting from the forward and the backward integration. The skill of the  
 390 dynamical interpolation is evaluated on the testing data from the two-layer QG model and  
 391 used for comparison with linear and deep learning interpolation.

## 392 **3 Results**

393 We have explored various neural network architectures for the task of temporal SSH  
 394 interpolation, ranging from single hidden layer networks (FC) to convolutional networks  
 395 (VGG), to a more complex residual neural networks (ResNet) – all achieving skills com-  
 396 parable to or higher than the linear and dynamical interpolation methods (Table 1). Sub-  
 397 stantially decreasing neural network complexity leads to an only slight decrease in the skill  
 398 (e.g. compare experiment pairs [1, 2] or [6,10] in Table 1), while substantially increasing the  
 399 complexity does not significantly improve the skill (e.g. compare experiment pairs [3,4] or  
 400 [7,10] in Table 1). The highest skill of 0.75 is achieved by the ResNet architecture (Fig. 1)  
 401 with a total of 52 convolutional layers and about five million adjustable parameters, taking  
 402 about 1 hour to train on a Tesla T4 GPU on 200K data samples. We thus find the ResNet  
 403 architecture to be optimal for our tasks and we use it throughout the paper to present our  
 404 deep learning results, although we note that other superior architectures may exist. Below  
 405 we use ResNet to demonstrate the deep learning skill in spatiotemporal SSH interpolation  
 406 and state estimation.

### 407 **3.1 Spatiotemporal SSH interpolation**

408 Upon training separate ResNets to perform temporal and spatiotemporal interpolation  
 409 of SSH data, a significant performance skill is achieved with networks generating realistic  
 410 SSH images with small errors (see Figure 4). The average prediction skill for both simu-  
 411 lations plateaus at about 0.75 and it isn't significantly smaller when evaluated on the test  
 412 dataset (Figure 3a). A few illustrative examples of eddy field evolution are shown in Fig-  
 413 ure 4a, demonstrating the non-trivial SSH evolution that occurs in a chaotic QG model of  
 414 baroclinically unstable flow. In the top-row example of Figure 4a, the strong positive SSH  
 415 anomaly in the center of the domain almost completely disappears after 20 days, yet the  
 416 neural network is still capable to reconstruct the SSH state at day 10. For such examples  
 417 when the eddy field changes dramatically with time, linear or objective interpolation tech-

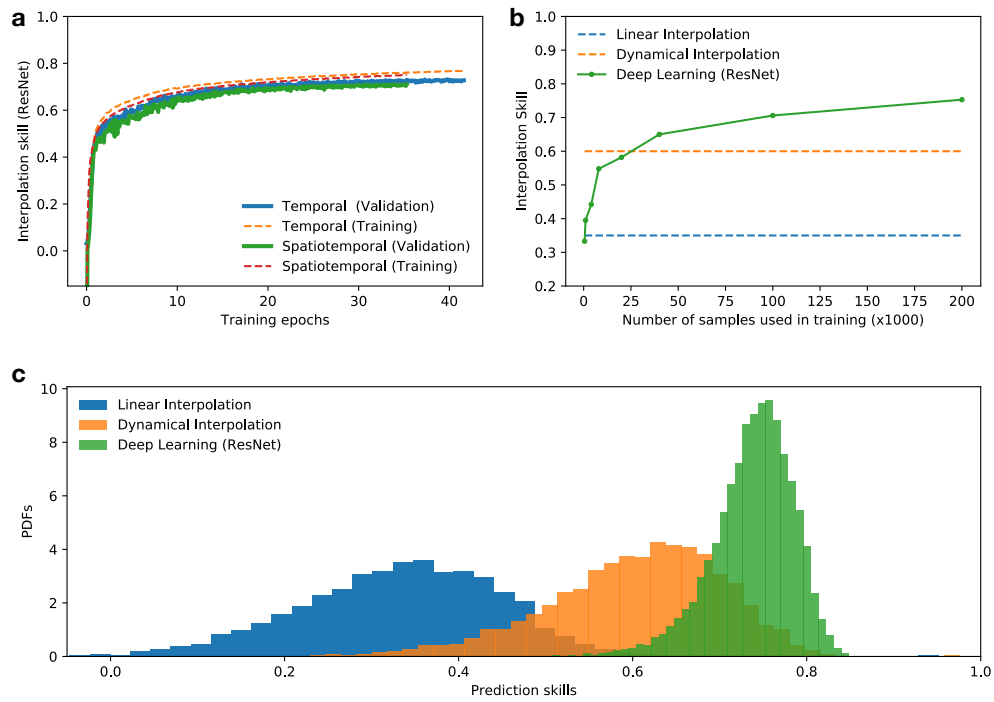


**Figure 3.** Performance comparison of the deep learning neural network (ResNet) with linear and dynamical interpolation techniques. (a) The evolution of the ResNet model validation and training skill during its training on temporal and spatiotemporal SSH interpolation (b) The dependence of the ResNet skill on the number of data samples used in training for the temporal SSH interpolation. (c) Comparison of skill distributions of the linear interpolation (LI), dynamical interpolation (DI), and the deep learning method evaluated on the testing dataset.

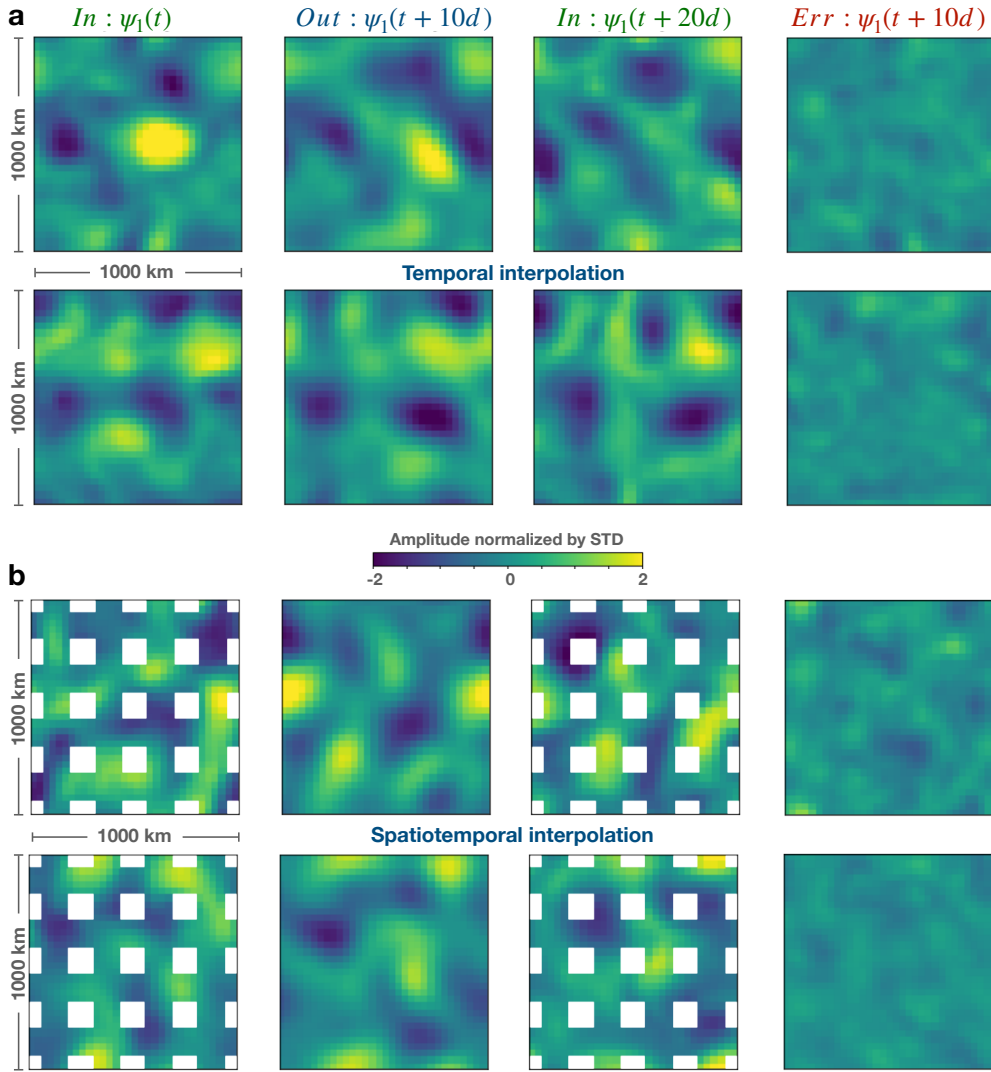


**Figure 4.** Examples of temporal (a) and spatiotemporal (b) interpolation of SSH data using the Deep Learning framework. Each row represents a randomly chosen interpolation example from the testing dataset. All panels share the same color bar and display streamfunction magnitudes normalized by the standard deviation of the entire dataset. The first and third column show panels with input SSH fields  $\psi_1(t)$  and  $\psi_1(t+20d)$ , second column shows the interpolated field  $\psi_1(t+10d)$ , and the fourth column shows the interpolation error. White regions in the case of spatiotemporal interpolation denote areas of obstructed input data.

418 niques perform poorly as they do not rely on any dynamical model of SSH evolution and  
 419 only make use of autocorrelation as a statistical model. Evaluated on a large number of  
 420 testing data (10K samples), the deep learning model outperforms the linear and dynamical  
 421 interpolation techniques, having not only a better average skill but also much more infre-  
 422 quent occurrence of low-skill interpolations, i.e. much narrower skill-distribution tail in the  
 423 direction of small skills (Figure 3c). Noticeably, the linear interpolation skills can be so low  
 424 as to approach zero and even negative values, i.e. its prediction is no better than assuming  
 425 that  $SSH = 0$  everywhere in the domain. The dynamical interpolation is much better than

426 the linear interpolation but still has a significant probability of poor interpolations in the  
427 skill range of about 0.4-0.6.

428 While the deep learning technique is superior to other methods, it is important to note  
429 that it still does not provide a perfect reconstruction and has a limit in skill bounded by  
430 about 0.85 (Fig. 3c). The dynamical evolution of the ocean flow considered in our study  
431 is inherently chaotic, i.e. the phase-space trajectories become well-mixed to the extent  
432 that the sensitivity to initial conditions increases exponentially with time. Thus, if SSH  
433 snapshots of a turbulent eddy field are separated by sufficiently large time (greater than  
434 the characteristic Lyapunov exponent timescale), there should be no physical or statistical  
435 relationship between these snapshots and hence no interpolation technique could achieve a  
436 skill significantly above zero. Indeed, given the same neural network architecture and the  
437 same volume of training data, the interpolation skill deteriorates dramatically from 0.75 to  
438 0.44 and 0.18 as the time separation between the input SSH snapshots increases from 20 to  
439 40 and 60 days correspondingly (Table 1).

440 The sensitivity to the number of data samples used in training demonstrates that for  
441 the ResNet architecture, about 20-30K data samples are needed to achieve a skill compa-  
442 rable to the dynamical interpolation skill, and using a larger number of training samples  
443 leads to a significant skill improvement (Figure 3b). However, the skill continues to increase  
444 slowly with the number of samples (Figure 3b), with the best power-law fit for the case of  
445 20-day SSH separation being  $skill \sim N^{0.09}$ , where  $N$  is the number of training samples.  
446 Extrapolating the power-law would imply that achieving the perfect  $skill = 1$  would re-  
447 quire  $O(10^7)$  training samples – a number beyond what the author’s computing capabilities,  
448 though not impossible to reach on modern supercomputers. Nonetheless, estimating the  
449 necessary number of samples is only a hypothetical consideration as it is not clear if the  
450 power-law would remain the same with the increasing volume of data. In addition, it is not  
451 possible to exclude the existence of superior neural network architectures that could lead to  
452 faster convergence.

### 453 3.2 State estimation of the unobserved deep ocean flows at mesoscales

454 Here we assess the efficacy of the Deep Learning framework in addressing the state  
455 estimation problem, i.e. estimating all dynamical variables in the ocean turbulence model,  
456 which in our case of a two-layer QG model implies estimating both the surface stream  
457 function  $\psi_1$  (or equivalently SSH) and the deep ocean streamfunction  $\psi_2$ . Conventionally,  
458 for state estimation, one needs to postulate the dynamical model and only then implement  
459 the techniques e.g. variational data assimilation or the ensemble Kalman filter techniques  
460 to estimate the unknown variables and parameters in the model at all times and everywhere  
461 within the model domain. However, we demonstrate here that the deep learning framework  
462 can provide an alternative to conventional data assimilation methods. The neural network  
463 is capable of skillful reconstruction of  $\tilde{\psi}_2$  based on two SSH snapshots separated by 20  
464 days, with an average skill of 0.7 for day 0 and a skill of 0.8 for day 20 (Figure 5). While  
465 the neural network provides skillful predictions for all state variables with skills ranging  
466 from 0.65 to 0.85, the best prediction skill is achieved for the deep flow at day 20 while  
467 the worst prediction is for deep flow at day 0 (compare orange and red curves in Fig5c).  
468 This temporal asymmetry is expected in chaotic and dissipative quasigeostrophic dynamics,  
469 making it more difficult to estimate the past state by observing the future as opposed to  
470 estimating the future by observing the past. Thus, the two SSH snapshots must indeed be  
471 ordered in time as the PV-evolution equations allow time reversal only for sufficiently small  
472 time intervals at which the dissipation effects can be neglected.

473 It is important to note that only the component of  $\psi_2$  that is uncorrelated with  $\psi_1$  can  
474 affect the SSH evolution because the tendency due to the advection of the surface stream-  
475 function by the surface flow is identically zero (see Eq. 5). However,  $\psi_2$  is highly correlated  
476 with  $\psi_1$ , with an average correlation coefficient is about 0.84, which is why reconstructing



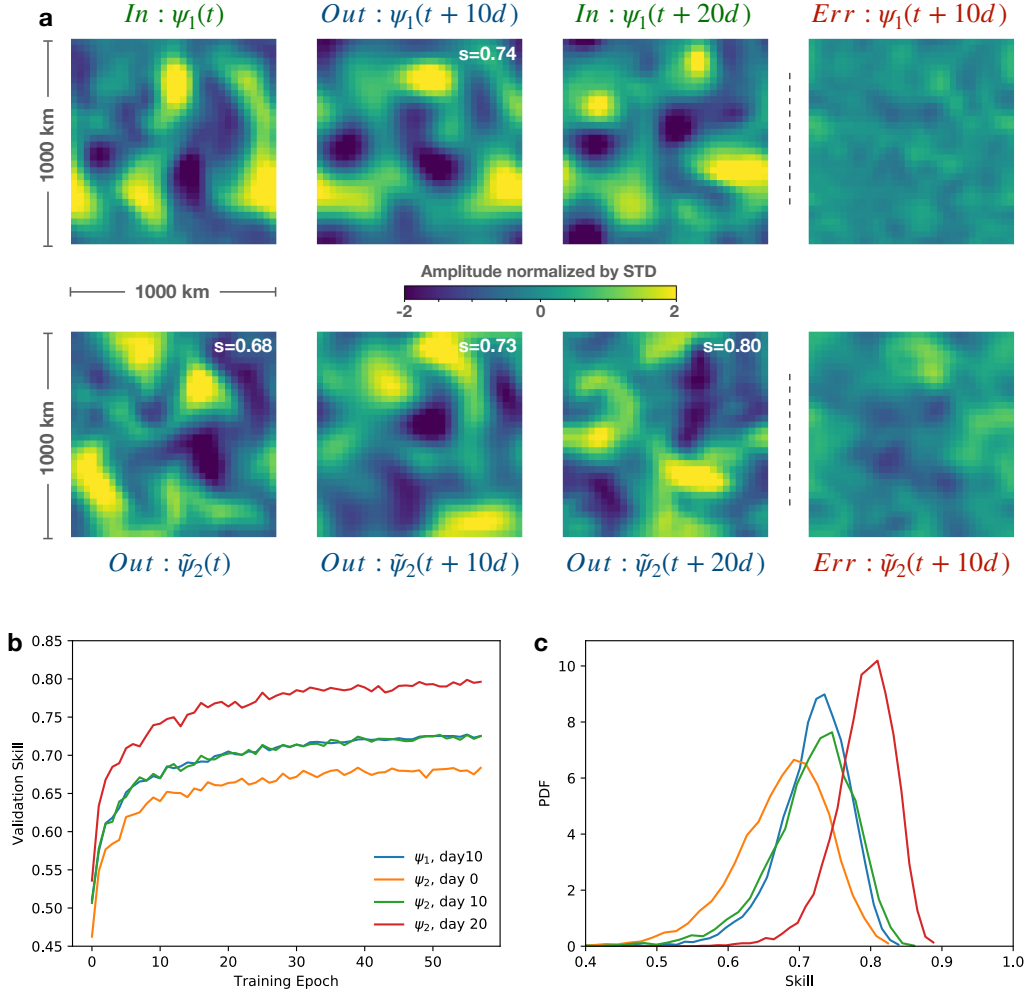


**Figure 5.** Examples of state estimation using Deep Learning neural network (a) and its statistical skill distribution for surface and subsurface variables at different times (b). As in the case of SSH interpolation, the neural network receives as input two SSH snapshots separated by 20 days,  $\psi_1(t)$  and  $\psi_1(t+20d)$  (top row, first and third columns), but reconstructs not only the surface streamfunction at the intermediate time,  $\psi_1(t+10d)$  (top row, second column), but also the subsurface flow at all three times:  $t$ ,  $t+10d$ , and  $t+20d$ . Note that  $\psi_1$  and  $\psi_2$  are linearly correlated with a correlation coefficient of 0.8, which is why the bottom rows in panel (a) show  $\tilde{\psi}_2$ , the component of the reconstructed deep flow that is not linearly correlated with the surface flow. The errors for reconstructing the day 10 surface and deep streamfunctions are shown in the last column. The probability density function of the neural network skill distribution is plotted in panel (b) for all predicted variables.

477 its full amplitude is a relatively trivial exercise. To evaluate the network ability to predict  
 478 the decorrelated component, we define it as  $\tilde{\psi}_2 = \psi_2 - A\psi_1$ , where the constant  $A$  is the  
 479 average linear regression coefficient between  $\psi_1$  and  $\psi_2$ . Indeed, using two SSH snapshots as  
 480 the input, the neural network does provide a skillful estimate of  $\tilde{\psi}_2$  with a relatively small  
 481 error (Fig5a). However, further exploring the limits of neural networks, we identify that  
 482 they are capable of reconstructing an instantaneous relation between the SSH field and deep  
 483 ocean streamfunction. We train the ResNet model using a single SSH snapshot as the input  
 484 and the decorrelated component  $\tilde{\psi}_2$  of the corresponding deep ocean streamfunction as the  
 485 output to achieve a prediction skill of 0.56, while a skill of 0.7 is achieved if using  $\psi_2$  as the  
 486 output.

## 487 4 Discussion

488 Our study explored the efficacy of deep learning in reconstructing the unobserved state  
 489 variables of the chaotic ocean turbulence. The motivation for addressing the specific problem  
 490 of SSH interpolation came from the present-day use of relatively rudimentary techniques of  
 491 reconstructing continuous fields from sparse satellite data. Using synthetic data from an  
 492 idealized model of baroclinic ocean turbulence, we presented the proof of concept for using  
 493 deep neural networks as an efficient technique to extract non-trivial information from sparse  
 494 SSH observations. Specifically, we demonstrated that residual convolutional neural networks  
 495 can reconstruct SSH snapshots at the intermediate time between the 20 days separated  
 496 observations with an average skill of 0.75, significantly outperforming the commonly used  
 497 linear interpolation (skill=0.35) and dynamical interpolation (skill=0.6) techniques. We  
 498 also demonstrated that the deep learning technique is flexible enough to address a more  
 499 general problem of state estimation that includes reconstruction of the unobserved deep  
 500 ocean streamfunction using only SSH snapshots. Nonetheless, there is an inherent lack of  
 501 information in SSH-only observations that prevents any interpolation or state estimation  
 502 methodology from achieving a perfect skill. After all, if SSH snapshots are separated by  
 503 a sufficiently long time, there should not be any relation between them due to the chaotic  
 504 nature of baroclinic ocean turbulence. Indeed, the ResNet could only achieve a maximum  
 505 skill of about 0.85 for interpolation between SSH snapshots separated by 20 days, and the  
 506 skill dramatically decreased to about 0.2 for the snapshots separated by 60 days. The lack  
 507 of the perfect interpolation skill suggests the existence of a dynamical barrier associated  
 508 with the inherent lack of information in SSH data, although it is not possible to deduce  
 509 this with certainty due to potential deficiencies of the neural network architecture and the  
 510 limited volume of training data.

511 While it is challenging to interpret the SSH interpolation algorithm that was ultimately  
 512 learned by the deep neural network, its superiority over other methods could be associated  
 513 with its ability to estimate the unobserved deep currents because they directly affect the  
 514 SSH evolution (Eq. 5). Taking only a surface streamfunction snapshot as the input, we  
 515 demonstrated that the ResNet can estimate the underlying deep ocean streamfunction with  
 516 an average skill of 0.7, which is high enough for a skillful estimate of the component of the  
 517 deep streamfunction that is not linearly correlated with the surface streamfunction. Apart  
 518 from deep learning, no other methods have been reported in the literature that can skillfully  
 519 estimate the uncorrelated component of the deep ocean currents at mesoscales. The success  
 520 of those neural network architectures that rely specifically on 2D convolutions for pattern  
 521 extraction implies that it may be the eddy shapes that contain the information necessary  
 522 to infer deep ocean currents.

523 A possible physical interpretation in terms of the eddy shapes could be drawn from  
 524 considering the ocean dynamics in terms of the barotropic and baroclinic modes that are  
 525 nonlinearly coupled and continuously exchange energy (Larichev & Held, 1995). The sur-  
 526 face streamfunction (or SSH) is simply the weighted sum of the barotropic and baroclinic  
 527 modes while the lower layer streamfunction is their difference. The key question here is: are  
 528 instantaneous observations of only surface streamfunction sufficient enough to reconstruct

529 the corresponding barotropic and baroclinic modes? This presents an under-constrained  
530 problem as there are two unknown modes while there is only one equation connecting their  
531 sum to the SSH field and there are no analytical laws that could be inferred from the QG  
532 dynamics to provide any additional constraints on the instantaneous relationship between  
533 the modes. Nonetheless, the distinct dynamical evolution of each mode can lead to dif-  
534 ferences in their characteristic spatial patterns that could be discerned by deep learning  
535 algorithms. The baroclinic mode experiences a direct energy cascade and its spatial struc-  
536 tures should appear more elliptical or elongated because it is stirred by the barotropic flow,  
537 especially at scales of the order of or smaller than the Rossby deformation radius. On the  
538 contrary, the barotropic mode experiences an inverse kinetic energy cascade manifested in  
539 eddy merging and a tendency towards axisymmetrization (Melander et al., 1987). While  
540 the two modes continuously interact by exchanging energy, the barotropic mode ends up  
541 strongly dominating the baroclinic mode at large scales and their amplitudes become com-  
542 parable at scales of the order of the Rossby deformation radius (see Figure 4a in Larichev &  
543 Held, 1995). This implies that the barotropic mode should dominate large-scale relatively  
544 axisymmetric eddy patterns, the baroclinic mode dominates smaller-scale relatively more el-  
545 liptical patterns, while both modes are present at the deformation scale. Thus, our tentative  
546 rationalization of the deep learning success is that by using convolutional filters, the neural  
547 networks are effectively extracting SSH patterns at different length scales and classifying  
548 them into barotropic and baroclinic modes. After estimating the mode amplitudes based on  
549 individual SSH snapshots and learning from many synthetic examples of SSH evolution in  
550 time, the neural networks are then capable to effectively integrate the QG equations forward  
551 or backward in time for a skillful temporal interpolation between the two SSH snapshots.  
552 While the complexity of deep learning algorithms makes it impossible to interpret them,  
553 our hypothetical two-step process of the mode decomposition followed by the forward and  
554 backward integration provides a plausible dynamical rationalization for the superiority of  
555 deep learning over methods that ignore the influence of deep ocean flows on SSH evolution.

556 We chose to use the quasigeostrophic simulations of baroclinic turbulence as the syn-  
557 thetic training dataset because it presents a hard test for the temporal SSH interpolation due  
558 to its chaotic nature and an a priori unknown impact of the dynamically active bottom layer  
559 on SSH evolution. However, for the case of submesoscale turbulence (length scales smaller  
560 than about 100 km), the question remains open as to how SWOT’s 2D high-resolution  
561 swath measurements could be used to enhance the resolution of SSH data. While we ex-  
562 pect the deep learning framework to perform well in reconstructing both large and small  
563 mesoscale eddies, its limitations still need to be understood when considering mesoscale  
564 and submesoscale turbulence as a continuum. It is thus necessary to develop more general  
565 training datasets that are representative of the SSH dynamics for any given region or pro-  
566 cess of interest. Including satellite observations from Synthetic Aperture Radars or of sea  
567 surface temperatures in addition to the SSH observations could provide additional informa-  
568 tion for improved reconstruction of SSH. The training datasets could be assembled ranging  
569 from more realistic submesoscale-resolving general circulation models to simplified stochas-  
570 tic models in various parameter regimes (Samelson et al., 2019). While diversifying the  
571 training datasets should increase the versatility of neural network interpolation methods,  
572 the crucial constraint of their performance would likely come from the chaotic evolution of  
573 submesoscale eddies that occurs on substantially shorter timescales compared to mesoscale  
574 eddies.

575 While we have demonstrated the efficacy of supervised deep learning using synthetic  
576 data, its practical utility in interpolating real-world SSH observations remains to be tested.  
577 The drawback of deep learning is that it requires a large volume of training data, although  
578 there are continuously improving methods aimed at addressing this practical issue, e.g.  
579 transfer learning (Pan & Yang, 2009), data augmentation (Perez & Wang, 2017), one-shot  
580 learning (Fei-Fei et al., 2006). A way towards ultimately developing the gridded SSH product  
581 using deep learning could be through training networks on a wide range of idealized and  
582 realistic models and then fine-tuning a much smaller number of neural network parameters

583 using existing satellite data. However, since the true two-dimensional SSH state is not known  
584 at any particular time, the fine-tuning of a neural network cannot be achieved by defining a  
585 simple loss function as was done with synthetic data. Thus, the neural network ultimately  
586 would need to use a loss function that is based purely on observations, without invoking a  
587 dynamical model to provide a true state. This issue could be addressed for example using  
588 reinforcement learning, where two-dimensional SSH fields generated by the neural network  
589 would be rewarded or penalized based on the accuracy of their projection on the observed  
590 altimetry tracks that were left out from the input set of tracks. Developing deep learning  
591 SSH interpolation techniques that would steer away from solely relying on dynamical models  
592 to provide training data is a necessary next step towards practical implementation with real  
593 satellite observations. Nonetheless, our work presents an important proof of concept that  
594 SSH observations do contain dynamically-relevant information about subsurface flows, and  
595 hence with deep learning it should be possible to build a skillful model of SSH evolution  
596 and as a consequence improve the existing SSH estimates.

597 Finally, we note another potentially important application of deep learning for state  
598 estimation at eddy-resolving scales. Since mesoscale-resolving data assimilation methods  
599 require large computations, providing an accurate initial guess would substantially reduce  
600 the number of iterations necessary for optimization. Thus, it might be possible to acceler-  
601 ate data assimilation methods by providing a deep learning estimate as a first guess that  
602 is already close to reality. Note that data assimilation and neural networks are similar  
603 approaches in that they both use iterative procedures to find the optimal set of unknown  
604 parameters to minimize the error between the predicted and true fields. The critical dif-  
605 ference is that data assimilation methods are based on a concrete physical model or its  
606 linearization, and hence the predicted fields conform to the desired physical constraints but  
607 the reconstruction skill relies on the accuracy of the model. Contrarily, the deep learning  
608 approach does not rely on a physical model as it is optimizing a complex non-linear mapping  
609 function that is general enough to map the input to the output. Hence, the deep learning  
610 predictions do not have to obey any dynamical constraints unless those have been explicitly  
611 incorporated in the loss function. Thus, we see the synergy between deep learning and  
612 conventional state estimation methods as a potential framework for constructing improved  
613 state estimates, combining the best of the two paradigms: fast data-driven state estimation  
614 via deep learning and fine-tuning by conventional data assimilation methods to ensure the  
615 strict consistency with an assumed dynamical model.

### 616 **Data Availability**

617 The neural network architectures coded in Tensorflow/Keras and the training datasets are  
618 published in the following Zenodo repository: <https://doi.org/10.5281/zenodo.3757524>

### 619 **Acknowledgments**

620 G.E.M. thanks Charles Trimble for providing support at the California Institute of Technol-  
621 ogy. L.S. and P.K. acknowledge support from NASA. Discussions with Andrew Thompson,  
622 Clement Ubelmann, Laure Zanna, and participants of the 2019 SWOT Science Team Meet-  
623 ing are highly appreciated. The authors thank Glenn Flierl for providing the Matlab code for  
624 simulating the two-layer quasigeostrophic turbulence and Michael Dietz for the open-source  
625 implementation of ResNet, modifications of which were used in this study.

### 626 **References**

- 627 Abernathey, R. P., & Marshall, J. (2013). Global surface eddy diffusivities derived from  
628 satellite altimetry. *Journal of Geophysical Research: Oceans*, *118*(2), 901–916.
- 629 Aluie, H., Hecht, M., & Vallis, G. K. (2018). Mapping the energy cascade in the north  
630 atlantic ocean: The coarse-graining approach. *Journal of Physical Oceanography*, *48*(2),  
631 225–244.
- 632 Arbic, B. K., Scott, R. B., Flierl, G. R., Morten, A. J., Richman, J. G., & Shriver, J. F.

- 633 (2012). Nonlinear cascades of surface oceanic geostrophic kinetic energy in the frequency  
634 domain. *Journal of Physical Oceanography*, *42*(9), 1577–1600.
- 635 Berloff, P. S., & Meacham, S. P. (1997). The dynamics of an equivalent-barotropic model  
636 of the wind-driven circulation. *Journal of marine research*, *55*(3), 407–451.
- 637 Bolton, T., & Zanna, L. (2019). Applications of deep learning to ocean data inference  
638 and subgrid parameterization. *Journal of Advances in Modeling Earth Systems*, *11*(1),  
639 376–399.
- 640 Carton, J. A., & Giese, B. S. (2008). A reanalysis of ocean climate using simple ocean data  
641 assimilation (soda). *Monthly Weather Review*, *136*(8), 2999–3017.
- 642 Chapman, C., & Charantonis, A. A. (2017). Reconstruction of subsurface velocities from  
643 satellite observations using iterative self-organizing maps. *IEEE Geoscience and Remote  
644 Sensing Letters*, *14*(5), 617–620.
- 645 Chelton, D. B., & Schlax, M. G. (2003). The accuracies of smoothed sea surface height  
646 fields constructed from tandem satellite altimeter datasets. *Journal of Atmospheric and  
647 Oceanic Technology*, *20*(9), 1276–1302.
- 648 Chelton, D. B., Schlax, M. G., & Samelson, R. M. (2011). Global observations of nonlinear  
649 mesoscale eddies. *Progress in Oceanography*, *91*(2), 167–216.
- 650 Davis, R. E. (1985). Objective mapping by least squares fitting. *Journal of Geophysical  
651 Research: Oceans*, *90*(C3), 4773–4777.
- 652 de La Lama, M. S., LaCasce, J. H., & Fuhr, H. K. (2016, 09). The vertical structure  
653 of ocean eddies. *Dynamics and Statistics of the Climate System*, *1*(1). Retrieved from  
654 <https://doi.org/10.1093/climsys/dzw001> (dzw001) doi: 10.1093/climsys/dzw001
- 655 Ducet, N., Le Traon, P.-Y., & Reverdin, G. (2000). Global high-resolution mapping of  
656 ocean circulation from topex/poseidon and ers-1 and-2. *Journal of Geophysical Research:  
657 Oceans*, *105*(C8), 19477–19498.
- 658 Fei-Fei, L., Fergus, R., & Perona, P. (2006). One-shot learning of object categories. *IEEE  
659 transactions on pattern analysis and machine intelligence*, *28*(4), 594–611.
- 660 Ferrari, R., & Wunsch, C. (2009). Ocean circulation kinetic energy: Reservoirs, sources,  
661 and sinks. *Annual Review of Fluid Mechanics*, *41*, 253–282.
- 662 Flierl, G. R. (1978). Models of vertical structure and the calibration of two-layer models.  
663 *Dynamics of Atmospheres and Oceans*, *2*(4), 341–381.
- 664 Fu, L.-L., Chelton, D. B., Le Traon, P.-Y., & Morrow, R. (2010). Eddy dynamics from  
665 satellite altimetry. *Oceanography*, *23*(4), 14–25.
- 666 Fu, L.-L., & Ubelmann, C. (2014). On the transition from profile altimeter to swath  
667 altimeter for observing global ocean surface topography. *Journal of Atmospheric and  
668 Oceanic Technology*, *31*(2), 560–568.
- 669 Gaultier, L., Ubelmann, C., & Fu, L.-L. (2016). The challenge of using future swot data  
670 for oceanic field reconstruction. *Journal of Atmospheric and Oceanic Technology*, *33*(1),  
671 119–126.
- 672 George, T., Manucharyan, G., & Thompson, A. (2019, Nov). *Deep learning to infer eddy heat  
673 fluxes from sea surface height patterns of mesoscale turbulence*. EarthArXiv. Retrieved  
674 from [eartharxiv.org/erhy2](https://eartharxiv.org/erhy2) doi: 10.31223/osf.io/erhy2
- 675 He, K., Zhang, X., Ren, S., & Sun, J. (2016). Deep residual learning for image recognition.  
676 In *Proceedings of the IEEE conference on computer vision and pattern recognition* (pp.  
677 770–778).
- 678 Kingma, D. P., & Ba, J. (2014). Adam: A method for stochastic optimization. *arXiv  
679 preprint arXiv:1412.6980*.
- 680 Klein, P., Isern-Fontanet, J., Lapeyre, G., Roulet, G., Danioux, E., Chapron, B., . . . Sasaki,  
681 H. (2009). Diagnosis of vertical velocities in the upper ocean from high resolution sea  
682 surface height. *Geophysical Research Letters*, *36*(12).
- 683 Klein, P., Lapeyre, G., Siegelman, L., Qiu, B., Fu, L.-L., Torres, H., . . . Le Gentil, S. (2019).  
684 Ocean-scale interactions from space. *Earth and Space Science*, *6*(5), 795–817.
- 685 Larichev, V. D., & Held, I. M. (1995). Eddy amplitudes and fluxes in a homogeneous  
686 model of fully developed baroclinic instability. *Journal of physical oceanography*, *25*(10),

- 687 2285–2297.
- 688 Le Traon, P., Nadal, F., & Ducet, N. (1998). An improved mapping method of multisatellite  
689 altimeter data. *Journal of atmospheric and oceanic technology*, *15*(2), 522–534.
- 690 Manucharyan, G. (2020, April). *State estimation of surface and deep flows from sparse SSH*  
691 *observations of geostrophic ocean turbulence using Deep Learning*. Zenodo. Retrieved  
692 from <https://doi.org/10.5281/zenodo.3757524> doi: 10.5281/zenodo.3757524
- 693 Melander, M., McWilliams, J., & Zabusky, N. (1987). Axisymmetrization and vorticity-  
694 gradient intensification of an isolated two-dimensional vortex through filamentation. *Jour-*  
695 *nal of Fluid Mechanics*, *178*, 137–159.
- 696 Pan, S. J., & Yang, Q. (2009). A survey on transfer learning. *IEEE Transactions on*  
697 *knowledge and data engineering*, *22*(10), 1345–1359.
- 698 Perez, L., & Wang, J. (2017). The effectiveness of data augmentation in image classification  
699 using deep learning. *arXiv preprint arXiv:1712.04621*.
- 700 Phillips, N. A. (1951). A simple three-dimensional model for the study of large-scale  
701 extratropical flow patterns. *Journal of Meteorology*, *8*(6), 381–394.
- 702 Samelson, R., Chelton, D., & Schlax, M. (2019). The ocean mesoscale regime of the  
703 reduced-gravity quasi-geostrophic model. *Journal of Physical Oceanography*(2019).
- 704 Scott, R. B., & Arbic, B. K. (2007). Spectral energy fluxes in geostrophic turbulence:  
705 Implications for ocean energetics. *Journal of physical oceanography*, *37*(3), 673–688.
- 706 Smith, K. S., & Vallis, G. K. (2001). The scales and equilibration of midocean eddies:  
707 Freely evolving flow. *Journal of Physical Oceanography*, *31*(2), 554–571.
- 708 Targ, S., Almeida, D., & Lyman, K. (2016). Resnet in resnet: Generalizing residual archi-  
709 tectures. *arXiv preprint arXiv:1603.08029*.
- 710 Ubelmann, C., Cornuelle, B., & Fu, L.-L. (2016). Dynamic mapping of along-track ocean al-  
711 timetry: method and performance from observing system simulation experiments. *Journal*  
712 *of Atmospheric and Oceanic Technology*, *33*(8), 1691–1699.
- 713 Ubelmann, C., Klein, P., & Fu, L.-L. (2015). Dynamic interpolation of sea surface height  
714 and potential applications for future high-resolution altimetry mapping. *Journal of At-*  
715 *mospheric and Oceanic Technology*, *32*(1), 177–184.
- 716 Vallis, G. K. (2017). *Atmospheric and oceanic fluid dynamics*. Cambridge University Press.
- 717 Wunsch, C. (1997). The vertical partition of oceanic horizontal kinetic energy. *Journal of*  
718 *Physical Oceanography*, *27*(8), 1770–1794.
- 719 Wunsch, C. (2010). Toward a midlatitude ocean frequency–wavenumber spectral density  
720 and trend determination. *Journal of Physical Oceanography*, *40*(10), 2264–2281.